Journal of Alloys and Compounds 813 (2020) 152235

Contents lists available at ScienceDirect

Journal of Alloys and Compounds

journal homepage: http://www.elsevier.com/locate/jalcom

Spray pyrolysis synthesis and characterization of $Mg_{1-x}Sr_xMoO_4$ heterostructure with white light emission

A.A.G. Santiago [a, *], R.L. Tranquilin [a], P. Botella [b], F.J. Manjón [c], D. Errandonea [d], C.A. Paskocimas [a], F.V. Motta [a], M.R.D. Bomio [a]

[a] LSQM, Laboratory of Chemical Synthesis of Materials, Department of Materials Engineering, Federal University of Rio Grande do Norte, UFRN, P.O. Box 1524, Natal, RN, Brazil
[b] Department of Engineering Sciences and Mathematics Luleå University of Technology, SE-97187, Luleå, Sweden
[c] Instituto de Diseño para la Fabricación y Producción Automatizada, MALTA Consolider Team, Universitat Politècnica de València, València, Spain
[d] Departamento de Física Aplicada-ICMUV, Universidad de Valencia, MALTA Consolider Team, Edificio de Investigación, C. Dr. Moliner 50, 46100, Burjassot, Spain

ARTICLE INFO

Article history:
Received 3 May 2019
Received in revised form
6 September 2019
Accepted 10 September 2019
Available online 10 September 2019

Keywords:
Ultrasonic spray pyrolysis
Raman spectroscopy
Photoluminescence
Molybdate
White emission

ABSTRACT

Molybdates are inorganic materials with great potential in white phosphors application, being an alternative to traditional lighting sources. In this study, we report the synthesis and characterization of $Mg_{1-x}Sr_xMoO_4$ ($x = 0$, 0.25, 0.50, 0.75, and 1) powders with white light-emitting properties. Using X-ray diffraction, the formation of the monoclinic β-$MgMoO_4$ phase was observed for $x = 0$ and the formation of the tetragonal scheelite phase of $SrMoO_4$ was observed for $x = 1$. The formation of a heterostructure composed of both phases was found for compositions with $x = 0.25$, 0.50 and 0.75. Scanning and trasmission electron microscopy images showed that the $Mg_{1-x}Sr_xMoO_4$ particles exhibit a spherical morphology formed by several primary nanoparticles. Raman scattering spectroscopy enabled the accurate identification of the Raman modes for different compositions and their assignment to either the $SrMoO_4$ or β-$MgMoO_4$ modes. The bandgap energies were determined to fluctuate between 4.25 eV and 4.44 eV, being influenced by the degree of structural disorder. The photoluminescence emission spectra of the nanoparticles showed neutral- and cool-white emission with high-quality white light (CRI > 80%). The samples synthesized with $x \leq 0.50$ are potential materials for the application in LED lamps (6500 K) and pure white-light sources (5500 K).

1. Introduction

Since its discovery, light-emitting diodes (LEDs) have been gradually replacing traditional lighting sources, such as incandescent and fluorescent lamps. LED enhancement studies have led to a considerable increase in luminous efficiency and also to discover materials with a better lifetime, lower energy consumption, greater stability, and which are environmentally friendly [1–4].

Generally, white light is achieved by using the combination of an InGaN chip (blue emission) and a YAG:Ce^{3+} phosphor (yellow emission), but this methodology results in high color temperature correlation (CCT) and low color rendering index (CRI) [5,6]. One of the alternatives used to obtain white light sources is the combination of phosphors doped with rare-earth elements that emit red, green, and blue light. These phosphors belong to several classes of materials, such as rare-earth oxides, molybdates, tungstates, silicates, phosphates, or niobates [7–9]. Unfortunately, the use of rare-earth elements in phosphors implies higher costs and increases the toxicological risk [10]. Thus, as an alternative technology, the synthesis of several materials by different routes using morphological and structural modifiers and forming heterostructures has been carried out in order to obtain white light emission phosphors without the use of rare-earth elements [11–14].

The ultrasonic spray pyrolysis (USP) method had shown to be an interesting route to obtain white-emitting photoluminescent materials because of the structural and morphological alterations achieved during the process [15–18]. Also, the USP method has other advantages such as the simplicity of equipment, a quick and single-step process, a non-complex precursor solution, and the

* Corresponding author.
E-mail address: andersonsantiago@ufrn.edu.br (A.A.G. Santiago).

https://doi.org/10.1016/j.jallcom.2019.152235
0925-8388/

formation of powders with high homogeneous and purity [19–22]. Recently, the USP method has been used to obtain different molybdates such as $NiMoO_4$ [23,24], $SrMoO_4$ [25], $La_2Mo_2O_9$ [26], $Na_2Mo_2O_7$ [27], and $CoMoO_4$ [28].

Molybdates are inorganic materials that have great potential in different applications such as phosphors, supercapacitors, scintillators, and photocatalysis [29–35]. Among the molybdates, magnesium molybdate ($MgMoO_4$) stands out because it has an efficient matrix to host other elements. The monoclinic structure of its β-phase is formed by two octahedral [MgO_6] and two tetrahedral [MoO_4] sites [36,37]. On the other hand, strontium molybdate ($SrMoO_4$) has a tetragonal scheelite-type structure formed by one dodecahedral [SrO_8] and one tetrahedral [MoO_4], resulting in a material with excellent thermal and chemical stability [38,39]. The photoluminescent properties of $MgMoO_4$ and $SrMoO_4$ have been recurrently studied, showing variations in: synthesis routes, such as microwave-assisted hydrothermal, solid-state reaction, combustion; and/or inserting different elements in the structure, such as Ba^{2+}, Tm^{3+}, Dy^{3+}, Yb^{3+}, Pr^{3+}, Eu^{3+}, Bi^{3+}, Li^{+}, Na^{+} or K^{+} [37,40–47]. However, studies about the structural and photoluminescence properties of the solid-solution formed between $MgMoO_4$ and $SrMoO_4$ structures are not found in the literature.

In this study we report the synthesis of $Mg_{1-x}Sr_xMoO_4$ (x = 0, 0.25, 0.5, 0.75, and 1) powder samples, prepared by the USP method, as well the characterization of their structural, morphological, vibrational, and optical properties at room conditions by means of x-ray diffraction (XRD), field-emission scanning electron microscopy (FESEM), transmission electron microscopy (TEM) and high-resolution transmission electron microscopy (HRTEM), Raman scattering (RS), photoluminescence (PL) and ultraviolet–visible (UV–Vis) reflectance measurements.

2. Experiment details

2.1. Materials

Magnesium nitrate hexahydrate [$Mg(NO_3)_2 \cdot 6H_2O$] (98.0% purity; Vetec), strontium nitrate [$Sr(NO_3)_2$] (99.0% purity, Vetec), molybdic acid [H_2MoO_4] (85% purity; Alfa Aesar), guanidine hydrochloride [$CH_5N_3 \cdot HCl$] (98.0% purity, Alfa Aesar), and distilled water were used as reagents to synthesize $Mg_{1-x}Sr_xMoO_4$.

2.2. The synthesis procedure of $Mg_{1-x}Sr_xMoO_4$ powders

Powder samples of $Mg_{1-x}Sr_xMoO_4$ (x = 0, 0.25, 0.5, 0.75, and 1), hereafter noted as MMO, MS25MO, MS50MO, MS75MO and SMO, respectively, were prepared by using the USP method [16,48]. The precursor solution for $MgMoO_4$ was prepared by dissolving 3.75 mmol of magnesium nitrate, 3.75 mmol of molybdic acid, and 0.75 mmol of guanidine hydrochloride in 150 ml of distilled water under magnetic stirring at 25 °C. The precursor solution was atomized using an ultrasonic nebulizer (frequency of 2.4 MHz) with an airflow of 3 L min^{-1} and the heating temperatures were from 600 °C for zone 1 and 800 °C for zone 2. More details on the equipment and implemented technique are listed in Ref. [15]. The other precursor solutions were made according to the stoichiometry shown in Table 1.

2.3. Characterization of $Mg_{1-x}Sr_xMoO_4$ powders

Powder XRD patterns of $Mg_{1-x}Sr_xMoO_4$ were collected within the 10° to 120° angular range with step speed of 0.02° min^{-1} using an XRD 7000 Shimadzu diffractometer and monochromatic Cu K_α (λ = 1.5406 Å) radiation. The diffraction patterns were analyzed by means of the General Structure Analysis System (GSAS) with graphic interface EXPGUI [49] in order to perform the Rietveld refinement [50] and to analyze the possible structural modifications. The following parameters were refined: scaling factor and phase fraction; background (displaced Chebyshev polynomial function); peak shape (Thomson-Cox-Hasting pseudo-Voigt); change in the network constants; fractional atomic coordinates; and isotropic thermal parameters.

Table 1
Codes for $Mg_{1-x}Sr_xMoO_4$ powder samples with nominal concentration, x = 0, 0.25, 0.5, 0.75 and 1.

x ($Mg_{1-x}Sr_xMoO_4$)	Code
x = 0	MMO
x = 0.25	MS25MO
x = 0.5	MS50MO
x = 0.75	MS75MO
x = 1	SMO

The powder morphology was examined using a FESEM (Carl Zeiss, model Supra 35-VP) operating at 6 kV. Transmission electron microscopy (TEM) and high-resolution transmission electron microscopy (HRTEM) images were obtained with an FEI Tecnai G2 F20 microscope operating at 200 kV. The sample was initially prepared by using 20 mg of MS50MO dispersed in 3 mL of acetone via ultrasonication. The copper TEM grids with carbon film (3 nm) were rapidly submerged in this dispersion and then dried in a vacuum for 12 h.

Non-polarized RS measurements were carried out using a LabRAM HR UV coupled to a Peltier cooled CCD camera, using a 632.8 nm HeNe laser excitation line with a power smaller than 10 mW and a spectral resolution better than 2 cm^{-1}. Samples were checked before and after each RS measurement to ensure that no heating effects occurred during the measurements. RS spectra peaks were analyzed by fitting them to Voigt profiles where the spectrometer resolution is taken as the fixed Gaussian width.

The UV–Vis reflectance spectrum was obtained using a UV–Vis spectrometer (Shimadzu, model UV-2600) and PL spectra were measured using a Thermal Jarrell-Ash Monospec 27 monochromator and a Hamamatsu R446 photomultiplier. The excitation source used was a krypton laser with a wavelength of 325 nm (Coherent Innova) with an output of approximately 13.3 mW.

3. Results and discussion

3.1. Structural characterization

Powder XRD patterns of $Mg_{1-x}Sr_xMoO_4$ (x = 0, 0.25, 0.50, 0.75,

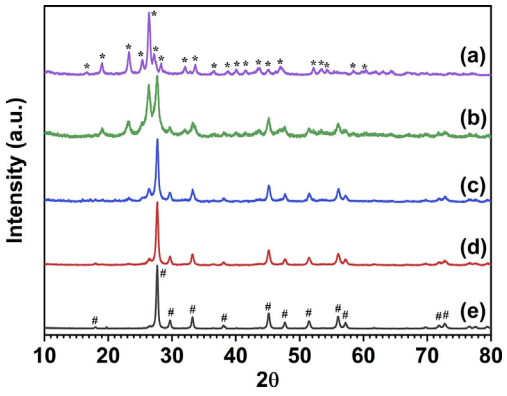

Fig. 1. XRD patterns of $Mg_{1-x}Sr_xMoO_4$ being (a) MMO, (b) MS25MO, (c) MS50MO, (d) MS75MO and (e) SMO. * is referent to JCPDS 21–096 and # is referent to JCPDS 85–0809. It is noted the tetragonal phase increases with increasing the value of x due to the increase in the substitution of Mg^{2+} cations by Sr^{2+} cations.

and 1) samples are shown in Fig. 1 and Fig. S1 (see Supporting Information). The MMO sample was indexed in a unit cell with a monoclinic structure (β-$MgMoO_4$ polymorph) with space group *C*2/*m* (number 12) in agreement with JCPDS 21–0961 and the literature [51,52]. The SMO sample was indexed in a unit cell with a tetragonal scheelite-type structure with space group $I4_1/a$ (number 88) in agreement with JCPDS 85–0809 and the literature [53,54]. The MS25MO, MS50MO, and MS75MO samples were indexed with JCPDS 21–096 and JCPDS 85–0809 cards, being observed the coexistence of all Bragg peaks of each structure. Note that the fraction of the tetragonal phase increases with increasing the value of x since there is an increase in the substitution of Mg^{2+} cations by Sr^{2+} cations in the heterostructure.

Fig. 2 and Table 2 show the results obtained from the Rietveld refinement of XRD patterns of the different samples. The XRD pattern of the MMO sample was well matched to ICSD 20418 (β-

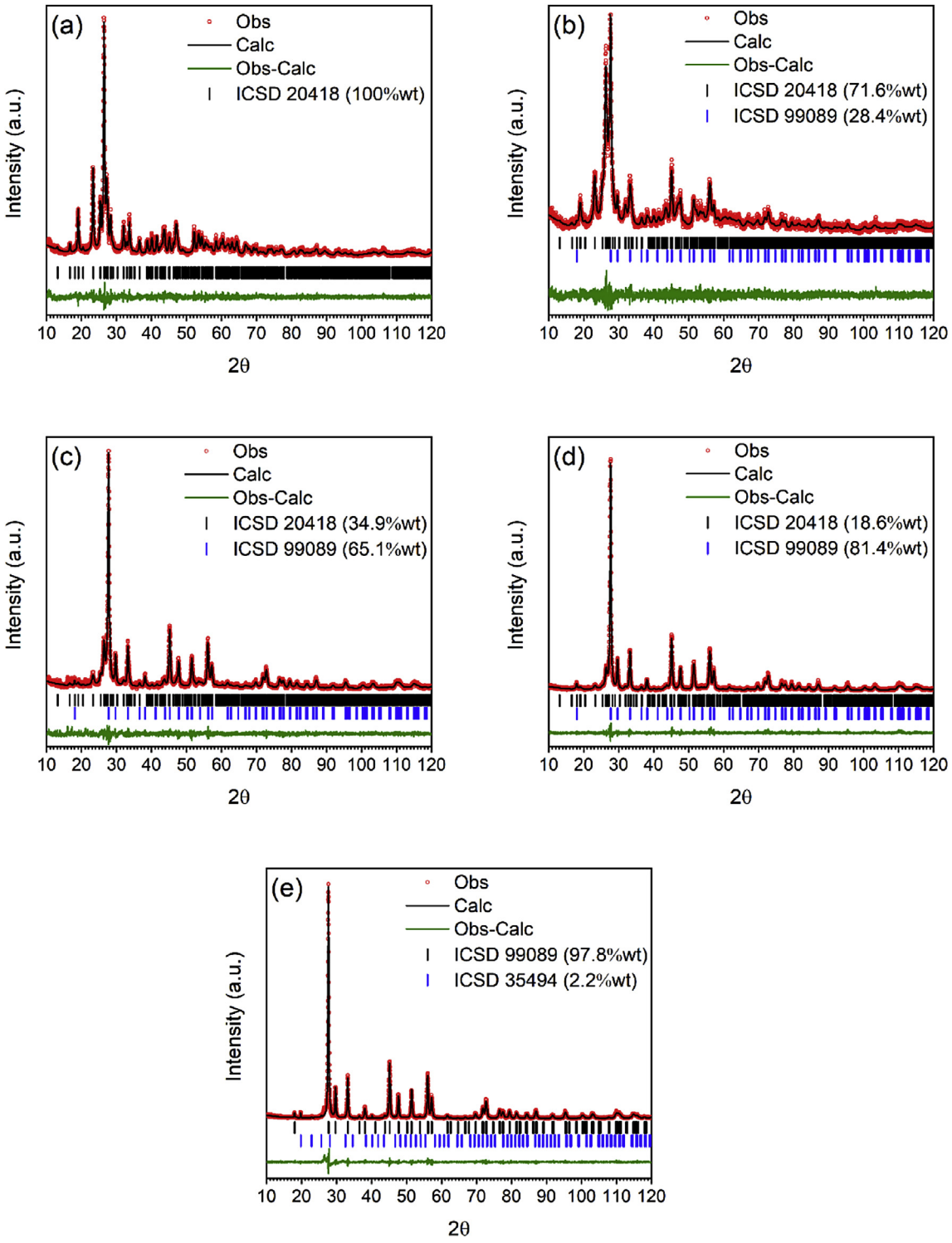

Fig. 2. Rietveld refinement of $Mg_{1-x}Sr_xMoO_4$ being (a) MMO, (b) MS25MO, (c) MS50MO, (d) MS75MO and (e) SMO.

Table 2
Rietveld refined structural parameters for the $Mg_{1-x}Sr_xMoO_4$ with x = 0, 0.25, 0.5, 0.75 and 1. Values between parentheses are estimation of error.

Compounds	MMO	MS25MO	MS25MO	MS50MO
Crystal system	Monoclinic	Monoclinic	Tetragonal	Monoclinic
Space Group	*C2/m*	*C2/m*	$I4_1/a$	*C2/m*
Lattice parameters (Å)				
a	10.27(3)	10.26(2)	5.390(6)	10.28(4)
b	9.296(7)	9.339(2)	–	9.312(3)
c	7.021(1)	7.020(2)	12.04(2)	7.020(3)
c/a	–	–	2.234	–
α	90°	90°	90°	90°
β	106.9(5)°	106.7(1)°	–	107.0(2)
γ	90°	90°	–	90°
$V(Å^3)$	641.7(8)	644.3(2)	349.9(7)	642.6(3)
χ^2	1.516	1.204	1.204	1.564
Rp (%)	9.96	9.29	9.29	9.77
RF^2 (%)	5.42	5.67	5.67	5.62
D (nm)	18.1	9.90	16.2	11.0
$\varepsilon\ (x10^{-3})$	1.30	2.39	1.40	2.35
Compounds	MS50MO	MS75MO	MS75MO	SMO
Crystal system	Tetragonal	Monoclinic	Tetragonal	Tetragonal
Space Group	$I4_1/a$	*C2/m*	$I4_1/a$	$I4_1/a$
Lattice parameters (Å)				
a	5.391(4)	10.29(9)	5.391(3)	5.395(5)
b	–	9.259(7)	–	–
c	12.03(3)	7.080(3)	12.03(2)	12.03(3)
c/a	2.232	–	2.232	2.234
α	90°	90°	90°	90°
β	–	107.2(7)	–	–
γ	–	90°	–	–
$V(Å^3)$	349.7(7)	645.1(6)	349.7(3)	350.1(8)
χ^2	1.564	1.416	1.416	1.622
Rp (%)	9.77	9.41	9.41	9.57
RF^2 (%)	5.62	10.57	10.57	4.62
D (nm)	16.2	8.10	15.9	20.8
$\varepsilon\ (x10^{-3})$	1.43	4.30	1.48	1.12

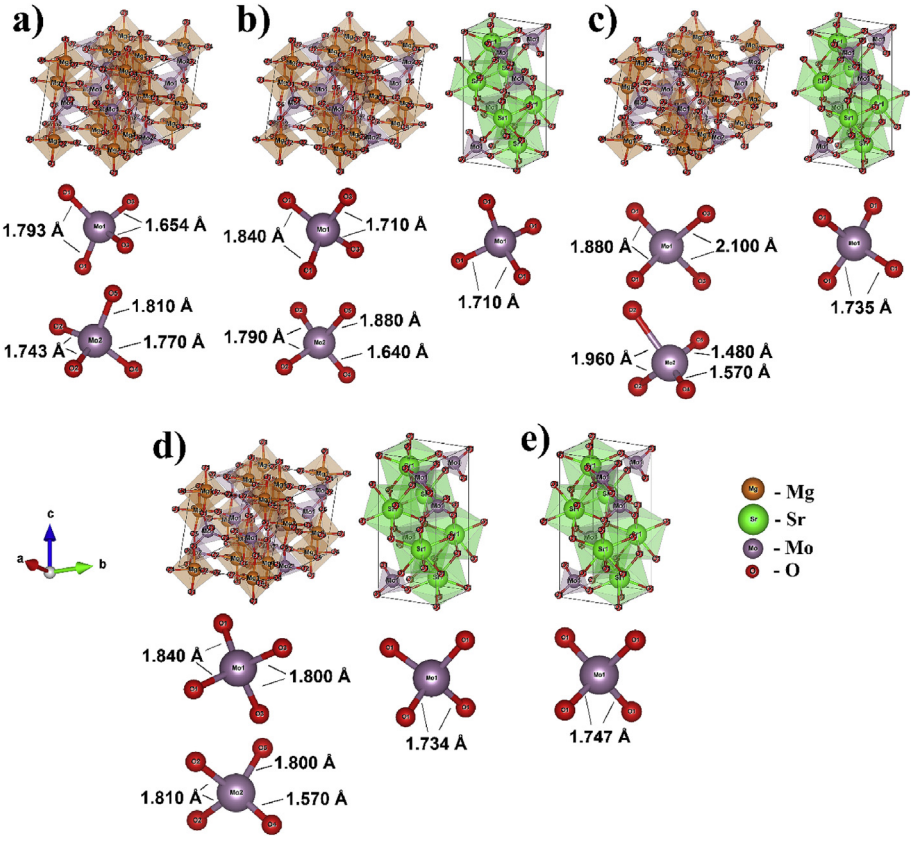

Fig. 3. Structural modeling of the $Mg_{1-x}Sr_xMoO_4$ being (a) MMO, monoclinic structure; (b) MS25MO, monoclinic and tetragonal structures; (c) MS50MO, monoclinic and tetragonal structures, (d) MS75MO, monoclinic and tetragonal structures and (e) SMO, tetragonal structure.

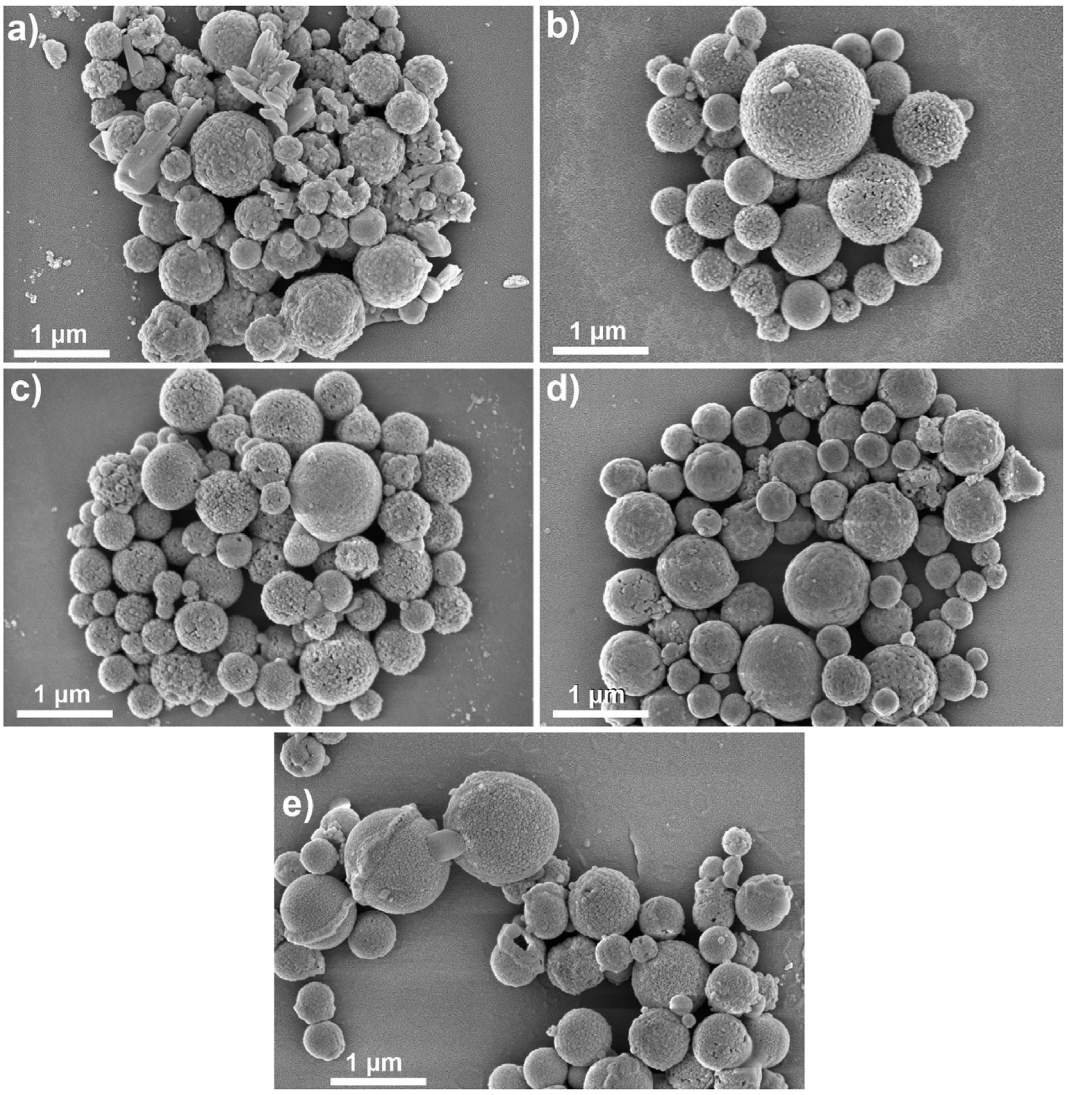

Fig. 4. FESEM micrographs of $Mg_{1-x}Sr_xMoO_4$ powders being (a) MMO, (b) MS25MO, (c) MS50MO, (d) MS75MO and (e) SMO.

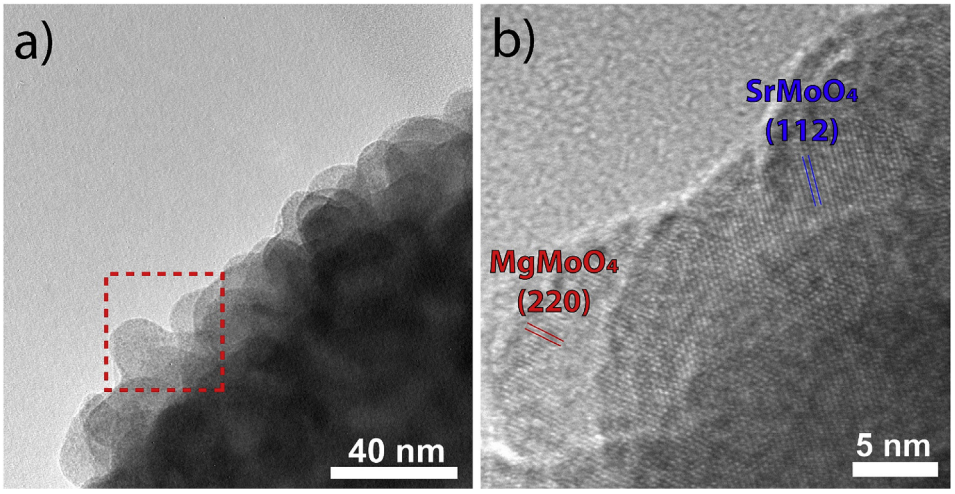

Fig. 5. (a) TEM and (b) HRTEM micrographs of MS50MO powder.

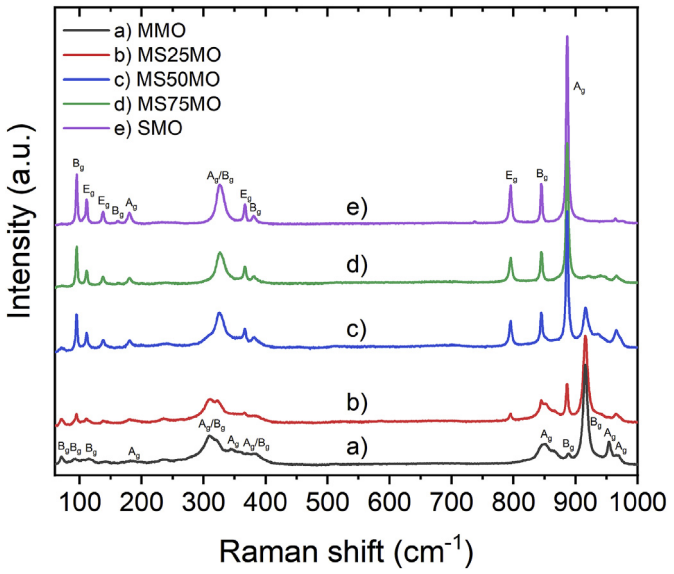

Fig. 6. Raman spectra of $Mg_{1-x}Sr_xMoO_4$ being (a) MMO, (b) MS25MO, (c) MS50MO, (d) MS75MO and (e) SMO.

$MgMoO_4$ with monoclinic structure). For the SMO sample, the diffraction pattern was well matched to ICSD 99809 ($SrMoO_4$ with tetragonal structure) and ICSD 35494 ($Sr(NO_3)_2$ with cubic structure), featuring 2.2%wt of strontium nitrate as an impurity, resulting from the incomplete decomposition of the precursor reagent during USP. Finally, MS25MO, MS50MO, and MS75MO samples were well matched to a combination of both ICSD 20418 and ICSD 99809, thereby forming a heterostructure.

Small changes in the structural parameters have been observed between samples, such as in the unit-cell parameter, crystallite size, and displacement of the atomic positions within the crystalline structure. These phenomena may be related to defects caused during the USP process which, generate oxygen vacancies, possible substitutions of Mg^{2+} ions for Sr^{2+} ions in the monoclinic structure and vice versa, distortions in the $[MoO_4]^{2-}$ clusters, and in the interface itself between the two heterostructure phases. Fig. 3 shows a representation of the unit cells of the different $Mg_{1-x}Sr_xMoO_4$ samples and the distortions in the $[MoO_4]^{2-}$ cluster for the different values of x.

3.2. Morphological characterization

Fig. 4 shows the FESEM micrographs of the $Mg_{1-x}Sr_xMoO_4$

Table 3
Raman modes measured in $Mg_{1-x}Sr_xMoO_4$ with x = 0, 0.25, 0.5, 0.75 and 1. The results for $MgMoO_4$ and $SrMoO_4$ are compared with results from the literature, denoted by *, shown in the first column for $MgMoO_4$ and in the last column for $SrMoO_4$.

$MgMoO_4$*	MMO	MS25MO	MS50MO	MS75MO	SMO	$SrMoO_4$*
42[a]						
69,71[a]	71	71	66	67		
74	74	74	71	73		
81	82					
89,90[a]	90	91	92			
97	94	95	95	95	95	98,98[b]
105, 106[a]	105	105	105	104		
119[a]		113	113	114	114	115,114[b]
121,121[a]	119	119	119			
		140	140	140	140	142,141[b]
155,156[a]	152	153	154	153		
158[a]				163	162	163,163[b]
178, 179[a]	181	180	181	181	180	184,182[b]
	188	189	191	193		
204,203[a],205[a]	204					
	236	236	237	238	236	236,236[b]
275,275[a], 280[a],290[a]	286	280				
308[a]	309	309	308	305		
324,322[a],324[a]	322	323	325	325	327	329,328[b]
332[a]		330	330	330	331	331
335,339[a]	335	336	337	337		
351,345[a],351[a]	353	352	352	353		
		366	366	367	366	368,369[b]
371,371[a]	371	373				
		383	382	381	381	382,384[b]
385,385[a]	385	386	387	388		
401,403[a]						
427,427[a]						
756,754[a]						
773,774[a]						
		795	795	795	795	798,797[b]
		844	845	845	845	848,846[b]
856,856[a]	849	850	849			
874,874[a]	876	877	879			
	888	888	888	888	888	889,888[b]
906,906[a]						
912,912[a]	916	916	916	920		
959,959[a]	954	954	946	948		
971,970[a]	968	966	966	966		

[a] Data of Miller [57] for $MgMoO_4$ and.
[b] Data of Jayaraman et al. [59] for $SrMoO_4$.

powder samples. The morphology of $Mg_{1-x}Sr_xMoO_4$ samples is predominantly formed by microspheres particles. In addition, small pores and holes are observed on the surface of the microspheres. The microspheres of MMO (Fig. 4a) exhibit slight distortion together with more apparent surface roughness. On the other hand, the microspheres of SMO (Fig. 4e) have a smoother surface with small distortions in the circumference of the microsphere. Thus, the MS25MO, MS50MO and MS75MO microspheres (Fig. 4b–d) show the variations in morphology between MMO and SMO. The variations in the morphology are related to the utilized precursor reagents due to the solubility in water and decomposition temperature.

Several physicochemical phenomena occur simultaneously in the USP process, such as evaporation of the solvent on the surface of

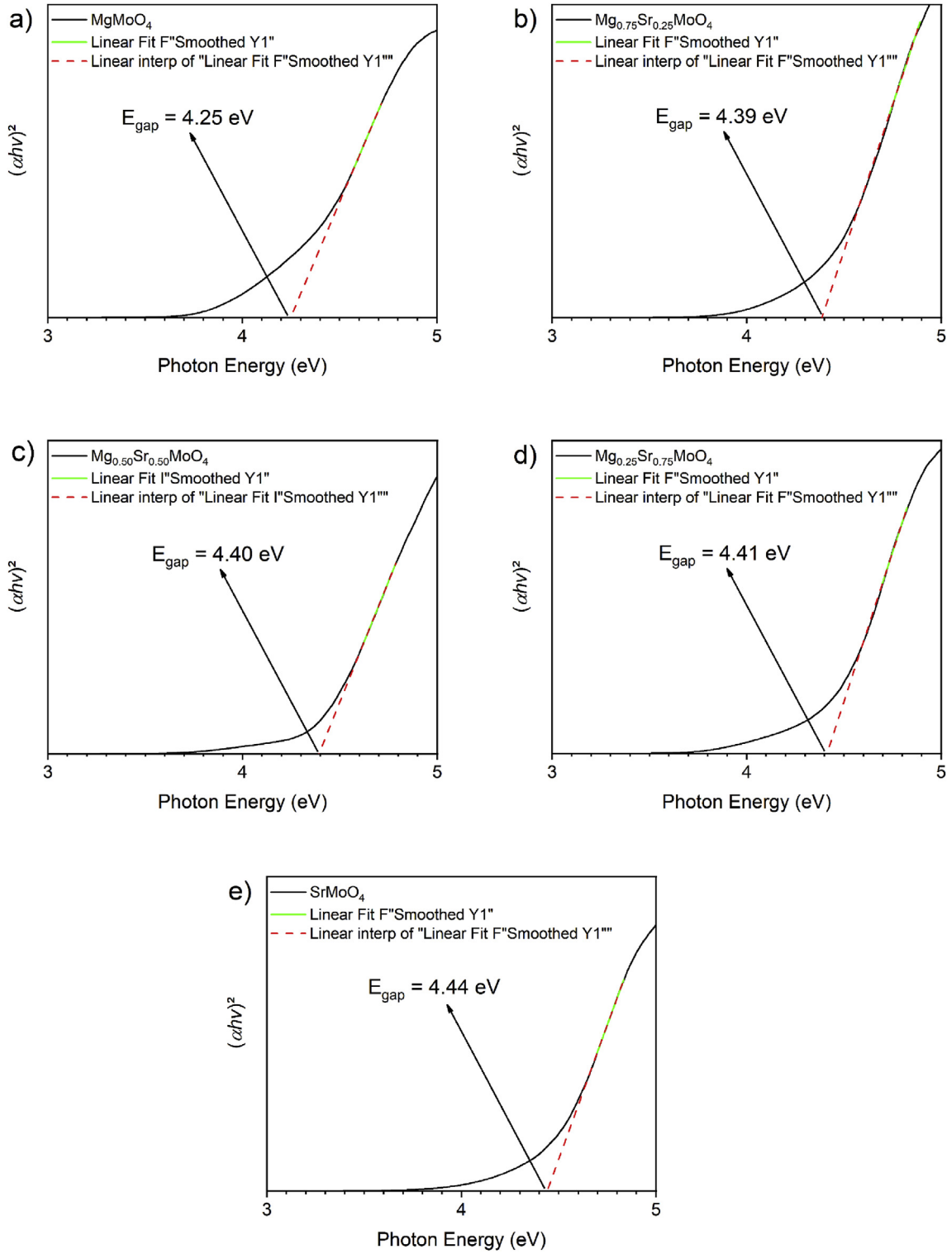

Fig. 7. UV–Vis absorbance spectra of $Mg_{1-x}Sr_xMoO_4$ being (a) MMO, (b) MS25MO, (c) MS50MO, (d) MS75MO and (e) SMO.

the droplet, the diffusion of solvent vapors away from the droplet in the gas phase, and the melting of metal nitrates. The metal nitrates tend to melt before the solvent is completely removed forming a molten salt and this molten salt prevents the solvent from being removed, thus giving rise to the porous or hollow microspheres [55].

Since metal nitrates were used for $Mg_{1-x}Sr_xMoO_4$ synthesis, and the result is the formation of porous and hollow microspheres with holes. In addition, metal nitrates generally tend to have a high degree of supersaturation and reagents with this characteristic tend to form a high number of nanosized crystallites that form the microspheres [55]. It is noted that the microspheres are formed by small particles of nanometric size, which joined together during the USP process. As the precursor reagents used were magnesium nitrate and strontium nitrate and present high solubility in water (0.71 g/ml of H_2O and 0.80 g/ml H_2O, respectively [56]), this favors the formation of nanocrystals which composes the microspheres that are observed.

The TEM and HRTEM were utilized for investing the nanocrystals composing the microspheres. The MS50MO particles are formed by microspheres composed of several nanoparticles, as seen in Fig. 5a. Moreover, the microsphere has the (220) plane of the $MgMoO_4$ and the (112) plane of the $SrMoO_4$ in the same particle (Fig. 5b). Thus, the presence of these planes and the interface between phases confirm the formation of the heterostructure.

3.3. Vibrational characterization

Fig. 6 shows the RS spectra measured in the different samples. We found that the spectra gradually change from the typical RS spectrum of monoclinic β-$MgMoO_4$ (bottom trace) to that expected in tetragonal scheelite-type $SrMoO_4$ (top trace). For intermediate compositions, we found the coexistence of the monoclinic and tetragonal end-member compounds. The intensity of the Raman modes gradually loses intensity as the content of Sr increases in the sample, gradually becoming the dominant Raman modes of $SrMoO_4$, as expected. In Table 3 we report the frequencies of the Raman modes observed in each sample. Group theory analysis predicts that monoclinic $MgMoO_4$ has 36 Raman-active modes ($19A_g + 17B_g$) and tetragonal scheelite-type $SrMoO_4$ has 13 Raman-active modes ($3\ A_g + 5B_g + 5E_g$).

In previous works, more than 25 Raman-active modes have been reported for MMO [57,58]. In our case, we have observed 25 modes, in which 20 of our modes agree within uncertainties with the frequencies reported in the literature (see Table 3). There are several weak modes reported by Miller [57] and by Coelho et al. [58] which we did not observe, and there are three weak modes that we found at 188, 236, and 889 cm^{-1} which have not been previously reported. The comparison with the works of Miller [57] and by Coelho et al. [58] indicates that all the modes we measured in MMO can be assigned to β-$MgMoO_4$. In total, 32 out of 36 Raman-active modes of MMO can be identified between ours and previous measurements.

In the case of SMO, the agreement with previous studies [59,60] is excellent (Table 3). For intermediate compositions, we found that the samples have the Raman modes of the two compounds, as expected for the prepared heterostructures. The mode frequencies are only slightly affected by the composition. In MS25MO, the presence of scheelite-type Raman modes of SMO in the high-frequency region is evident in Fig. 6e. Notice how these peaks and other new peaks gradually win intensity in Fig. 6, while the original MMO modes gradually lose intensity as the Sr content increases. However, the MMO Raman modes are still present in MS75MO, as can be clearly seen in the high-frequency region of Fig. 6.

There are a few interesting facts that we would like to remark on here. One is the decrease in the number of Raman modes in $SrMoO_4$ in comparison with β-$MgMoO_4$; a consequence of the increase in the symmetry of the tetragonal scheelite with respect to the monoclinic structure as well as in the decrease of the number of formula units in the primitive unit cell ($Z = 1$ in $SrMoO_4$ and $Z = 2$ in $MgMoO_4$). This is quite noticeable in the high-frequency region where only three modes (one doubly degenerated) are expected in SMO associated to the internal stretching vibrations of the MoO_4 tetrahedron. In contrast, eight internal modes are expected in the high-frequency region of MMO due to the presence of two different distorted MoO_4 tetrahedra. Another qualitative difference between the RS spectra of SMO and MMO is that the Raman modes in the high-frequency region corresponding to the stretching modes of the MoO_4 tetrahedra cover a much smaller frequency region (between 790 and 900 cm^{-1}) in SMO than in MMO, where high-frequency modes are found between 740 and 980 cm^{-1}. This is due to the same four Mo−O distances (~1.88 Å) in the regular MoO_4 tetrahedron of SMO in comparison to those of MMO where the two irregular MoO_4 tetrahedra show Mo−O distances in the range between 1.73 and 1.85 Å. In addition, the high-frequency Raman modes of SMO are much more intense than in MMO, with the high intensity of the SMO Raman modes being typical of scheelite-type oxides. These qualitative differences between the Raman spectra of both compounds enable accurate identification of the Raman modes of each phase in $Mg_{1-x}Sr_xMoO_4$ samples and their assignment to either SMO or MMO modes.

3.4. Optical characterization

3.4.1. UV−visible spectroscopy

Fig. 7 presents the estimated values for the band-gap energy of $Mg_{1-x}Sr_xMoO_4$ samples. UV−Vis spectroscopy was utilized for obtaining the diffuse reflectance data of samples and the gap energy values (*Egap*) were estimated using the Kubelka-Munk function [61] for converting the reflectance data to absorbance followed by the Wood and Tauc method [62]. The optical band-gap energy is assumed by $\alpha h\nu \propto (h\nu\text{-}E_{gap})^{1/k}$ [62], where α is the absorbance, h is the Planck constant, ν is the frequency, and k is indicated for the different kind of transitions. In the literature, molybdates are typically reported with permitted direct electronic transition [63−67], so the results from $Mg_{1-x}Sr_xMoO_4$ samples were analyzed assuming $k = 1/2$, which is the expected value for such transitions.

The estimated values for samples are according to the literature. Silva et al. [68] and Zhu et al. [45] synthesized $SrMoO_4$ and obtained

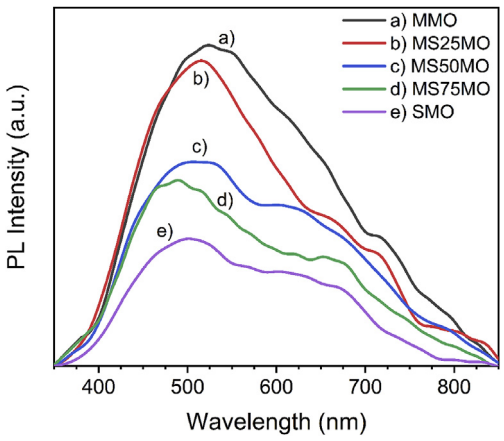

Fig. 8. PL spectra of $Mg_{1-x}Sr_xMoO_4$ being (a) MMO, (b) MS25MO, (c) MS50MO, (d) MS75MO and (e) SMO.

band gap values between 4.17 and 4.36 eV (agglomerates particles by complexation) and between 3.81 and 2.71 eV (nanoparticles by thermal decomposition), respectively. Wannapop et al. [69] and Zhang et al. [70] produced $MgMoO_4$ and estimated the band gap value of 5.15 eV (fibers via electrospinning) and between 3.72 and 3.78 eV (nano-flowers and nanosheets via self-assembly), respectively.

The molybdates have wide-bandgap values due to the low number of intermediary levels between the valence band and the conduction band. The band-gap is mainly determined by Mo 4d states and oxygen 2p states. This is the reason why (as occurs in tungstates) the bandgap only changes 0.2 eV from $MgMoO_4$ to $SrMoO_4$ [71]. In addition, the band-gap energy could be strongly influenced by the degree of order and structural disorder [72,73]. The greater the structural disorder, the lower the band-gap of molybdate will be due to the increase of intermediate levels. Sczancoski et al. [74] calculated the bandgap of $BaMoO_4$ and related the decrease in bandgap with the increase of defects due to increases of intermediary energy levels, being 4.93 eV for the material free of structural defects and 4.10 eV for the material with distorted

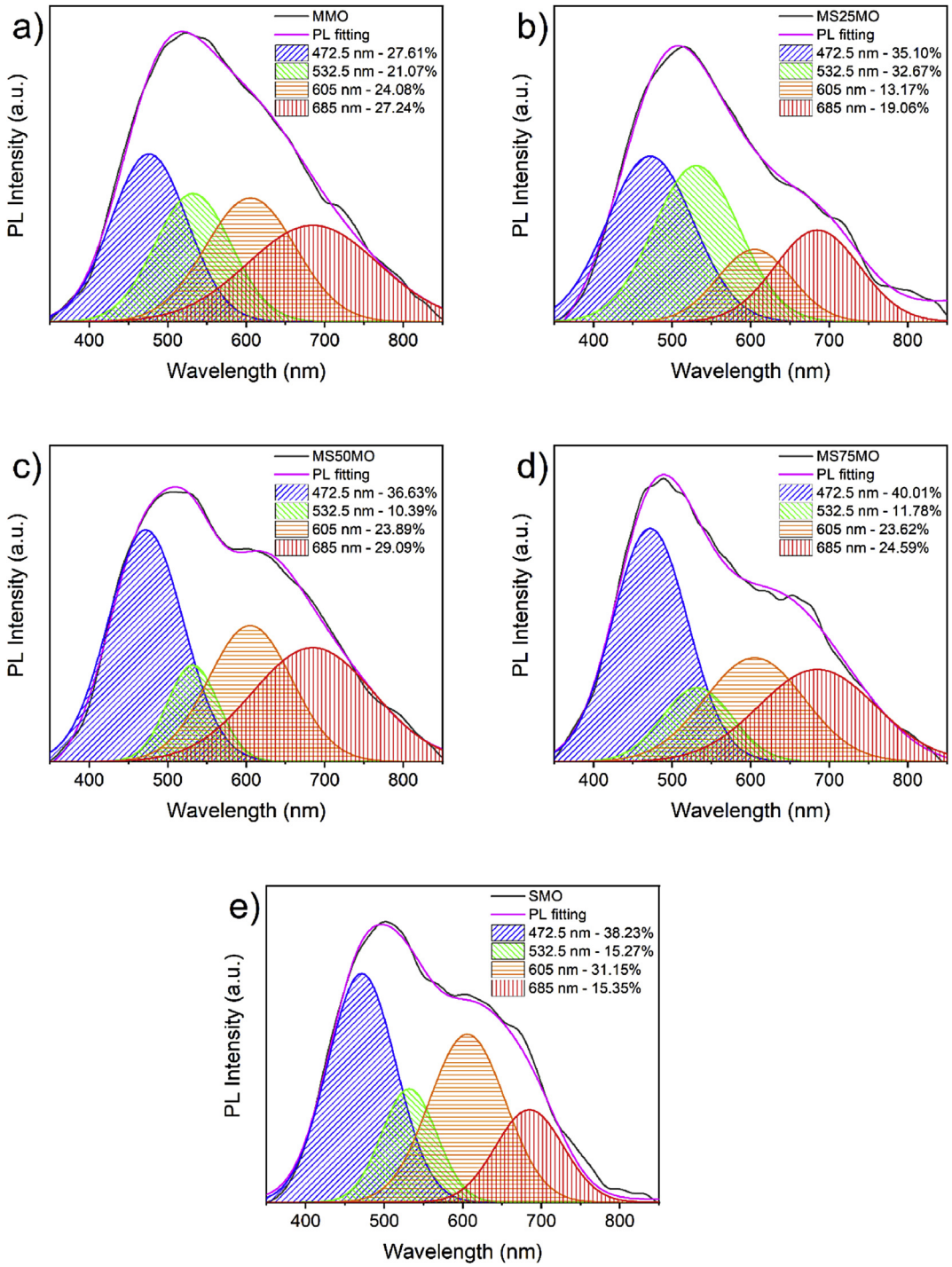

Fig. 9. PL deconvolution of $Mg_{1-x}Sr_xMoO_4$ being (a) MMO, (b) MS25MO, (c) MS50MO, (d) MS75MO and (e) SMO.

structure. Longo et al. [75] calculated the bandgap of $CaMoO_4$ and demonstrated than units cells ordered exhibit larger bandgap comparing to cells disordered (4.57 eV−2.57 eV, respectively). It is also reported that other factors may influence the bandgap of molybdates, such as distortion of $[MoO_4]^{-2}$ clusters, the formation of oxygen vacancies and growth mechanisms which may promote an increase of intermediate levels and decrease the bandgap [74,76,77].

The MMO sample (Fig. 7a) shows 4.25 eV, while SMO (Fig. 7e) presents 4.44 eV. However, the MS25MO, MS50MO and MS75MO samples have intermediate gap bands, but with greater proximity to the band-gap shown in the SMO. Thus, the SMO phase has a greater influence on the band-gap of the formed heterostructure than the MMO, even when the SMO presents a smaller phase amount. This result suggests the presence of a large band-gap bowing parameter in this solid solution.

3.4.2. Photoluminescence (PL)

The PL emission spectra of the $Mg_{1-x}Sr_xMoO_4$ (x = 0, 0.25, 0.5, 0.75, and 1) powders obtained by the USP method were obtained at room temperature (see Fig. 8). The PL emission spectra of the samples exhibit a broadband spectrum. This phenomenon occurs when the relaxation involves the participation of many states in several places within the band-gap of the material, and this is also known as a multiphonon and multilevel process [78].

The PL emission of molybdates is fundamentally related to the crystalline structure and the distortion of their polyhedral units. Intermediate levels appear within the molybdate band-gap when a molybdate is excited and there are distortions in its clusters $[MoO_4]$ because of the energy absorption of low-energy states (O 2p orbitals) and promotion of high energy states (Mo 4d orbitals) [79]. The PL emission colors are due to electronic transitions associated with the structural arrangements and cluster-to-cluster transfer charge, with the emission in the yellow-red region being associated with deep defects, structural disorder and oxygen vacancies in $[MoO_4]$ clusters, while the emission in the blue-green region associated with shallow defects and structural ordering, being the color emission association proven in literature by the thermoluminescence spectrum and EPR analysis [73,80–83]. Thus, the deconvolution of the Gaussian curves of $Mg_{1-x}Sr_xMoO_4$ samples was performed using the PeakFit 4.12 software to estimate the contribution of each color in the PL emission of the samples, as can be seen in Fig. 9.

The deconvolutions propose that all samples have a predominance of PL emission in the blue region. The MMO sample shows a small difference between the proportions of each color. Thus, it is believed that the color emission is generated by cluster-to-cluster transfer charge and the ratio between ordered $[MgO_6]_o/[MoO_4]_o$ clusters and disordered $[MgO_6]_d/[MoO_4]_d$ clusters, as presented in the following equations:

$$[MgO_6]_o^X + [MgO_6]_d^X \rightarrow [MgO_6]_o^{'} + [MgO_6]_d^{\bullet} \quad (1)$$

$$[MoO_4]_o^X + [MoO_4]_d^X \rightarrow [MoO_4]_o^{'} + [MoO_4]_d^{\bullet} \quad (2)$$

Meanwhile, the SMO sample shows a higher amount of blue and orange colors compared to green and red colors. It is believed that the emission of the colors follows the same line of thought as the MMO, but the emission occurs due to the ratio between ordered $[SrO_8]_o/[MoO_4]_o$ clusters and disordered $[SrO_8]_d/[MoO_4]_d$ clusters, as shown below:

$$[SrO_8]_o^X + [SrO_8]_d^X \rightarrow [SrO_8]_o^{'} + [SrO_8]_d^{\bullet} \quad (3)$$

$$[MoO_4]_o^X + [MoO_4]_d^X \rightarrow [MoO_4]_o^{'} + [MoO_4]_d^{\bullet} \quad (4)$$

On the other hand, if the value of x increases, the spectrum tends to change from the MMO spectrum to the SMO spectrum. This occurs due to the proportion of each phase within the heterostructure, as well as defects generated during the formation and charge transfer at the interface between the phases. Thus, it is believed that the color emission occurs due to the ratio between ordered $[MgO_6]_o/[SrO_8]_o/[MoO_4]_o$ clusters and disordered $[MgO_6]_d/[SrO_8]_d/[MoO_4]_d$ clusters, as follows:

$$[MgO_6]_o^X + [MgO_6]_d^X \rightarrow [MgO_6]_o^{'} + [MgO_6]_d^{\bullet} \quad (5)$$

$$[SrO_8]_o^X + [SrO_8]_d^X \rightarrow [SrO_8]_o^{'} + [SrO_8]_d^{\bullet} \quad (6)$$

$$[MoO_4]_o^X + [MoO_4]_d^X \rightarrow [MoO_4]_o^{'} + [MoO_4]_d^{\bullet} \quad (7)$$

The CIE chromatic coordinates were calculated by determining the x and y coordinates to verify the color emitted by the spectrum of samples. The CIE is an important factor for checking the performance of matches and is calculated by integrating the X, Y and Z values. The CIE (x, y) coordinates of $Mg_{1-x}Sr_xMoO_4$ samples (x = 0, 0.25, 0.5, 0.75 and 1) are shown in Fig. 10, while Table 4 lists the CIE coordinates values, correlation color temperature (CCT), color rendering indices (CRI) and the color emitted from each sample.

White LEDs which show light generation with CCT between 4000 and 8000 K have neutral- and cool-white emission, requiring high CRI values (>80) to achieve a high-quality white light source [84,85]. All $Mg_{1-x}Sr_xMoO_4$ samples demonstrated emission in the white region and showed CRI>80, so these materials can be considered as promising high-quality white light sources. Several studies have used the doping of rare earth elements in molybdates to generate white light. Adya et al. [86] obtained the $SrMoO_4$:(0.005 mol Eu, 0.01 mol Tm) by the coprecipitation method and the CCT response was 6863 K. In using the solid-state method, Cao et al. [87] obtained $Ca_{0.95}MoO_4$:0.05Sm^{3+} and presented CCT response of 5608 K and CRI of 92.1%. Ham et al. [88] synthesized $Ca_{0.8}La_{0.2-x}MoO_4$:xDy^{3+} with x = 0.01 and 0.05 by the hydrothermal method, in which the white light emission had CCT of 6429 K and 5555 K, respectively. Laguna et al. [89] used the precipitation method to obtain $CaMoO_4$:(0.35% Dy, 0.15% Eu) and had a response

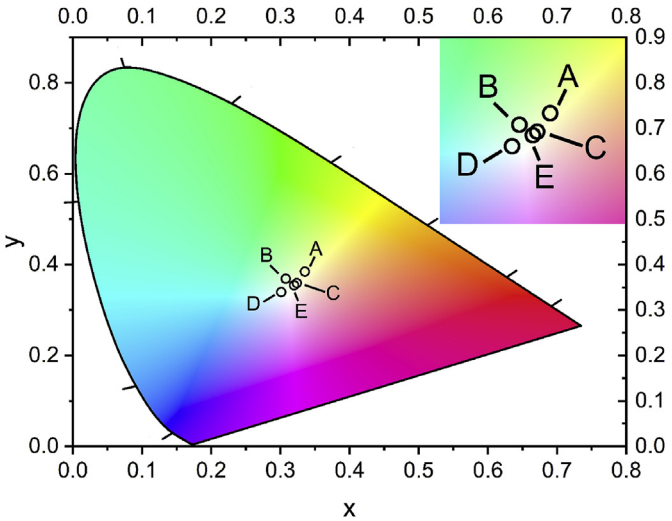

Fig. 10. CIE diagram of $Mg_{1-x}Sr_xMoO_4$ being (A) MMO, (B) MS25MO, (C) MS50MO, (D) MS75MO and (E) SMO.

Table 4
Chromaticity coordinates (CIE), correlated temperature color (CCT) and color rendering indices (CRI) for $Mg_{1-x}Sr_xMoO_4$.

Code	Sample	x	y	CCT	CRI (%)	Color
A	MMO	0.3354	0.3847	5411	88	Between daylight and sunlight
B	MS25MO	0.3077	0.3689	6481	85	Summer sunlight (and blue sky)
C	MS50MO	0.3238	0.3594	5852	96	Bright sunlight
D	MS75MO	0.3013	0.3394	7017	94	Light summer shade
E	SMO	0.3198	0.3546	5995	95	Bright sunlight

in white light with CCT of 5407 K. The toxicological significance of rare earth elements still needs to be explored, but studies show that prolonged exposure to RE dust can induce bronchiolar, alveolar and interstitial histological reactions in the lungs [90,91]. Thus, obtaining phosphors with white light emission that do not use RE have mainly been required for biological reasons. Consequently, the ultrasonic spray pyrolysis method has been shown to be an interesting route to obtain phosphors with white light emission without the use of rare earths materials, introducing simplicity and fast synthesis [15–17]. Therefore, the $Mg_{1-x}Sr_xMoO_4$ samples synthesized by the USP method have shown to be interesting in the application of LEDs, mainly for the MMO and MS50MO samples because they are close to the pure white CCT value (5500 K), and the MS25MO sample because of the CCT value being close to that of LED commercial lamps (6500 K).

4. Conclusion

$Mg_{1-x}Sr_xMoO_4$ (x = 0, 0.25, 0.50, 0.75, and 1) powders were successfully obtained by the ultrasonic spray pyrolysis method. XRD patterns showed that the sample with x = 0 has a monoclinic structure (β-$MgMoO_4$) and the sample with x = 1 has a scheelite tetragonal structure ($SrMoO_4$). On the other hand, the samples with x = 0.25, 0.5, and 0.75 showed the formation of a monoclinic/tetragonal heterostructure. The $Mg_{1-x}Sr_xMoO_4$ particles present spherical morphology with a rougher surface for x = 0 and a smoother surface for x = 1. The RS spectra enable qualifying and quantifying Raman modes of the $SrMoO_4$ or $MgMoO_4$ phases in $Mg_{1-x}Sr_xMoO_4$ samples. The band-gap of the sample with x = 0 (x = 1) was 4.25 eV (4.44 eV), while samples with x = 0.25, 0.50, and 0.75 showed intermediate values which seem to be highly influenced by the degree of structural disorder. The PL emission spectra of the samples showed a white emission composed of several bands. The color emission was attributed to cluster-to-cluster transfer charge and the ratio between ordered $[MgO_6]_o$/$[SrO_8]_o$/$[MoO_4]_o$ clusters and disordered $[MgO_6]_d$/$[SrO_8]_d$/$[MoO_4]_d$ clusters. All $Mg_{1-x}Sr_xMoO_4$ samples demonstrated emission in the white region with a CRI>80, and therefore these materials can be considered as promising high-quality white light sources.

Acknowledgments

The authors thank the following Brazilian and Spanish research financing institutions for financial support: A.A.G. Santiago acknowledges financial support from the National Council for Scientific and Technological Development - *CNPq*, the Graduate Program in Materials Science and Engineering (*PPGCEM-UFRN*) and the Coordination for the Improvement of Higher Education Personnel (*CAPES*) - Brazil (*CAPES*) - Finance Code 001. F.J.M. and D.E. acknowledge financial support from the Spanish *Ministerio de Ciencia, Innovación y Universidades*, the Spanish *Agencia Estatal de Investigacion* (*AEI*), and the *Fondo Europeo de Desarrollo Regional* (*FEDER*) under Grants No. MAT2016-75586-C4-1/2-P and from the *Generalitat Valenciana* under Grant Prometeo/2018/123 – *EFIMAT*.

Appendix A. Supplementary data

Supplementary data to this article can be found online at https://doi.org/10.1016/j.jallcom.2019.152235.

References

[1] Z. Gao, P. Sun, Y. Zhong, R. Yu, B. Deng, Eu^{3+}-doped highly thermal-stable barium yttrium aluminate as a red-emitting phosphor for UV based white LED, Opt. Laser. Technol. 111 (2019) 163–168.
[2] J. Zhong, X. Chen, D. Chen, M. Liu, Y. Zhu, X. Li, Z. Ji, A novel rare-earth free red-emitting $Li_3Mg_2SbO_6:Mn^{4+}$ phosphor-in-glass for warm w-LEDs: synthesis, structure, and luminescence properties, J. Alloy. Comp. 773 (2019) 413–422.
[3] J. Chen, Y. Liu, L. Mei, H. Liu, M. Fang, Z. Huang, Crystal structure and temperature-dependent luminescence characteristics of $KMg_4(PO_4)_3:Eu^{2+}$ phosphor for white light-emitting diodes, Sci. Rep. 5 (2015) 9673.
[4] P. Du, Y. Guo, S.H. Lee, J.S. Yu, Broad near-ultraviolet and blue excitation band induced dazzling red emissions in Eu^{3+}-activated Gd_2MoO_6 phosphors for white light-emitting diodes, RSC Adv. 7 (2017) 3170–3178.
[5] U. Farooq, Z. Zhao, Z. Sui, C. Gao, R. Dai, Z. Wang, Z. Zhang, Tm^{3+}/Dy^{3+}/Eu^{3+} (Sm^{3+}) tri-activated Y_2WO_6 as one potential single-phase phosphor for WLEDs, J. Alloy. Comp. 778 (2019) 942–950.
[6] U.B. Humayoun, S.B. Kwon, S.K. Sami, D.-H. Yoon, $(NH_4)_3AlF_6:Mn^{4+}$ a novel red phosphor – facile synthesis, structure and luminescence characteristics, J. Alloy. Comp. 776 (2019) 594–598.
[7] S. Yi, X. Hu, B. Liang, G. Hu, W. Zhao, Y. Wang, Synthesis and photoluminescence properties of Ln^{3+} (Ln^{3+} = Sm^{3+}/Eu^{3+}) doped Na_2NbAlO_5 phosphors, J. Lumin. 207 (2019) 105–113.
[8] C. Pan, X. Chen, G. Zhao, Y. Liu, Y. Li, Y. Fang, White-light-emitting from single-phased (Ca,Eu,Mn)$9Al(PO_4)_7$ phosphor with blue-white-yellow tunable luminescence properties for UV-based LEDs, Mater. Technol. 34 (2019) 135–142.
[9] M. Iwaki, S. Kumagai, S. Konishi, A. Koizumi, T. Hasegawa, K. Uematsu, A. Itadani, K. Toda, M. Sato, Blue-yellow multicolor phosphor, Eu^{2+}-activated Li_3NaSiO_4: excellent thermal stability and quenching mechanism, J. Alloy. Comp. 776 (2019) 1016–1024.
[10] X. Zheng, G. Ding, H. Wang, G. Cui, P. Zhang, One-step hydrothermal synthesis of carbon dots-polymer composites with solid-state photoluminescence, Mater. Lett. 238 (2019) 22–25.
[11] M. García-Tecedor, J. Bartolomé, D. Maestre, A. Trampert, A. Cremades, Li_2SnO_3 branched nano- and microstructures with intense and broadband white-light emission, Nano Res. 12 (2019) 441–448.
[12] Z. Wang, Z. Yang, Z. Yang, Q. Wei, Q. Zhou, L. Ma, X. Wang, Red phosphor $Rb_2NbOF_5:Mn^{4+}$ for warm white Light-Emitting Diodes with a high color-rendering index, Inorg. Chem. 58 (2019) 456–461.
[13] C. Ezquerro, E. Fresta, E. Serrano, E. Lalinde, J. García-Martínez, J.R. Berenguer, R.D. Costa, White-emitting organometallo-silica nanoparticles for sun-like light-emitting diodes, Mater. Horiz. 6 (2019) 130–136.
[14] A. Jorio, M.S. Dresselhaus, R. Saito, G. Dresselhaus, Raman Spectroscopy in Graphene Related Systems, John Wiley & Sons, 2011.
[15] A.A.G. Santiago, C.R.R. Almeida, R.L. Tranquilin, R.M. Nascimento, C.A. Paskocimas, E. Longo, F.V. Motta, M.R.D. Bomio, Photoluminescent properties of the $Ba_{1-x}Zn_xMoO_4$ heterostructure obtained by ultrasonic spray pyrolysis, Ceram. Int. 44 (2018) 3775–3786.
[16] C.R.R. Almeida, L.X. Lovisa, A.A.G. Santiago, M.S. Li, E. Longo, C.A. Paskocimas, F.V. Motta, M.R.D. Bomio, One-step synthesis of CaMoO4: Eu^{3+} nanospheres by ultrasonic spray pyrolysis, J. Mater. Sci. Mater. Electron. 28 (2017) 16867–16879.
[17] M.T.S. Tavares, M.M. Melo, V.D. Araújo, R.L. Tranquilin, C.R.R. Almeida, C.A. Paskocimas, M.R.D. Bomio, E. Longo, F.V. Motta, Enhancement of the photocatalytic activity and white emission of $CaIn_2O_4$ nanocrystals, J. Alloy. Comp. 658 (2016) 316–323.
[18] A.A.G. Santiago, Y.L.R.L. Fernandes, R.L. Tranquilin, E. Longo, C.A. Paskocimas, F.V. Motta, M.R.D. Bomio, Influence of $Zn_{1-x}Ca_xWO_4$ heterostructures synthesized by spray pyrolysis on photoluminescence property, Ceram. Int. (2019), https://doi.org/10.1016/j.ceramint.2019.08.022.
[19] J. Zheng, F. Song, S. Che, W. Li, Y. Ying, J. Yu, L. Qiao, One step synthesis process for fabricating $NiFe_2O_4$ nanoparticle loaded porous carbon spheres by ultrasonic spray pyrolysis, Adv. Powder Technol. 29 (2018) 1474–1480.
[20] S. Mao, R. Bao, D. Fang, J. Yi, Facile synthesis of Ag/AgX (X = Cl, Br) with

enhanced visible-light-induced photocatalytic activity by ultrasonic spray pyrolysis method, Adv. Powder Technol. 29 (2018) 2670–2677.
[21] X. Zhao, W. Li, F. Kong, H. Chen, Z. Wang, S. Liu, C. Jin, Carbon spheres derived from biomass residue via ultrasonic spray pyrolysis for supercapacitors, Mater. Chem. Phys. 219 (2018) 461–467.
[22] A.A.G. Santiago, L.X. Lovisa, P.N. Medeiros, M.S. Li, N.L.V. Carreño, E. Longo, C.A. Paskocimas, M.R.D. Bomio, F.V. Motta, Fast and simultaneous doping of $Sr_{0.9-x-y-z}Ca_{0.1}In_2O_4$:($xEu^{3+}$, yTm^{3+}, zTb^{3+}) superstructure by ultrasonic spray pyrolysis, Ultrason. Sonochem. 56 (2019) 14–24.
[23] G.D. Park, J.H. Hong, J.-K. Lee, Y.C. Kang, Yolk-shell-structured microspheres composed of N-doped-carbon-coated $NiMoO_4$ hollow nanospheres as superior performance anode materials for lithium-ion batteries, Nanoscale 11 (2019) 631–638.
[24] J.H. Ahn, G.D. Park, Y.C. Kang, J.-H. Lee, Phase-pure β-$NiMoO_4$ yolk-shell spheres for high-performance anode materials in lithium-ion batteries, Electrochim. Acta 174 (2015) 102–110.
[25] J.L. Wu, X. Wang, G.H. Peng, Z.H. Liang, X.F. Wang, Spherical $SrMoO_4$:Eu^{3+} phosphors prepared by spray pyrolysis, Adv. Mater. Res. 924 (2014) 93–97.
[26] L. Baqué, J. Vega-Castillo, S. Georges, A. Caneiro, E. Djurado, Microstructural and electrical characterizations of tungsten-doped $La_2Mo_2O_9$ prepared by spray pyrolysis, Ionics 19 (2013) 1761–1774.
[27] I.L. Validžić, M. Mitrić, Novel morphology of needle-Like nanoparticles of $Na_2Mo_2O_7$ synthesized by using ultrasonic spray pyrolysis, Mater. Res. 16 (2013) 44–49.
[28] Y.N. Ko, Y.C. Kang, S.B. Park, Superior cycling and rate performances of rattle-type $CoMoO_4$ microspheres prepared by one-pot spray pyrolysis, RSC Adv. 4 (2014) 17873–17878.
[29] Y. Tan, X. Luo, M. Mao, D. Shu, W. Shan, G. Li, D. Guo, Optimization red emission of $SrMoO_4$:Eu^{3+} via hydro-thermal co-precipitation synthesis using orthogonal experiment, Curr. Appl. Phys. 18 (2018) 1403–1409.
[30] S. Albohani, M. Minakshi Sundaram, D.W. Laird, Egg shell membrane template stabilises formation of β-$NiMoO_4$ nanowires and enhances hybrid supercapacitor behaviour, Mater. Lett. 236 (2019) 64–68.
[31] A.K.V. Raj, P. Prabhakar Rao, T.S. Sreena, T.R. Aju Thara, Broad greenish-yellow luminescence in $CaMoO_4$ by Si^{4+} acceptor doping as potential phosphors for white light emitting diode applications, J. Mater. Sci. Mater. Electron. 29 (2018) 16647–16653.
[32] I.R. Pandey, H.J. Kim, Y.D. Kim, Growth and characterization of $Na_2Mo_2O_7$ crystal scintillators for rare event searches, J. Cryst. Growth 480 (2017) 62–66.
[33] A.M. Huerta-Flores, I. Juárez-Ramírez, L.M. Torres-Martínez, J.E. Carrera-Crespo, T. Gómez-Bustamante, O. Sarabia-Ramos, Synthesis of $AMoO_4$ (A = Ca, Sr, Ba) photocatalysts and their potential application for hydrogen evolution and the degradation of tetracycline in water, J. Photochem. Photobiol. A Chem. 356 (2018) 29–37.
[34] D. Errandonea, D. Santamaria-Perez, S.N. Achary, A.K. Tyagi, P. Gall, P. Gougeon, High-pressure x-ray diffraction study of $CdMoO_4$ and $EuMoO_4$, J. Appl. Phys. 109 (2011), 043510-043510-043515.
[35] R. Vilaplana, O. Gomis, F.J. Manjón, P. Rodríguez-Hernández, A. Muñoz, D. Errandonea, S.N. Achary, A.K. Tyagi, Raman scattering study of bulk and nanocrystalline $PbMoO_4$ at high pressures, J. Appl. Phys. 112 (2012) 103510.
[36] L. Cornu, V. Jubera, A. Demourgues, G. Salek, M. Gaudon, Luminescence properties and pigment properties of A-doped (Zn,Mg)MoO_4 triclinic oxides (with A = Co, Ni, Cu or Mn), Ceram. Int. 43 (2017) 13377–13387.
[37] W. Ran, L. Wang, M. Yang, X. Kong, D. Qu, J. Shi, Enhanced energy transfer from Bi^{3+} to Eu^{3+} ions relying on the criss-cross cluster structure in $MgMoO_4$ phosphor, J. Lumin. 192 (2017) 141–147.
[38] A.K. Soni, M.K. Mahata, Photoluminescence and cathodoluminescence studies of Er^{3+}-activated strontium molybdate for solid-state lighting and display applications, Mater. Res. Express 4 (2017) 126201.
[39] F. Chun, W. Li, B. Zhang, W. Deng, X. Chu, H. Su, H. Osman, H. Zhang, X. Zhao, W. Yang, Visible and near-infrared luminescent properties of Pr^{3+} doped strontium molybdate thin films by a facile polymer-assisted deposition process, J. Colloid Interface Sci. 531 (2018) 181–188.
[40] L.-Y. Zhou, J.-S. Wei, L.-H. Yi, F.-Z. Gong, J.-L. Huang, W. Wang, A promising red phosphor $MgMoO_4$:Eu^{3+} for white light emitting diodes, Mater. Res. Bull. 44 (2009) 1411–1414.
[41] D.A. Spasskii, V.N. Kolobanov, V.V. Mikhaĭlin, L.Y. Berezovskaya, L.I. Ivleva, I.S. Voronina, Luminescence peculiarities and optical properties of $MgMoO_4$ and $MgMoO_4$:Yb crystals, Opt Spectrosc. 106 (2009) 556–563.
[42] Y.Q. Zhai, R.F. Li, X. Li, J.H. Li, Rapid synthesis and properties of color-tunable phosphors $SrMoO_4$:Eu^{3+},Tb^{3+}, Rare Met. 36 (2017) 828–832.
[43] F. Chun, B. Zhang, H. Su, H. Osman, W. Deng, W. Deng, H. Zhang, X. Zhao, W. Yang, Preparation and luminescent properties of self-organized broccoli-like $SrMoO_4$:Pr^{3+} superparticles, J. Lumin. 190 (2017) 69–75.
[44] Y. Wang, W. Wu, X. Fu, M. Liu, J. Cao, C. Shao, S. Chen, Metastable scheelite $CdWO_4$:Eu^{3+} nanophosphors: solvothermal synthesis, phase transitions and their polymorph-dependent luminescence properties, Dyes Pigments 147 (2017) 283–290.
[45] Y.N. Zhu, G.H. Zheng, Z.X. Dai, J.J. Mu, Z.F. Yao, Mono-disperse $SrMoO_4$ nanocrystals: synthesis, luminescence and photocatalysis, J. Mater. Sci. Technol. 33 (2017) 834–842.
[46] S.M.V. Paradelas, R.F. Gonçalves, F.V. Motta, R.C. Lima, M.S. Li, E. Longo, A.P.d.A. Marques, Effects of microwave-assisted hydrothermal treatment and of use of capping reagent on the photophysical properties of $SrMoO_4$ phosphors, J. Lumin. 192 (2017) 818–826.
[47] D. Zhu, C. Wang, F. Jiang, Preparation and luminescent properties of $Ba_{0.05}Sr_{0.95}MoO_4$: Tm^{3+} Dy^{3+} white-light phosphors, J. Lumin. 192 (2017) 1235–1241.
[48] P.N. Medeiros, A.A.G. Santiago, E.A.C. Ferreira, M.S. Li, E. Longo, M.R.D. Bomio, F.V. Motta, Influence Ca-doped $SrIn_2O_4$ powders on photoluminescence property prepared one step by ultrasonic spray pyrolysis, J. Alloy. Comp. 747 (2018) 1078–1087.
[49] B. Toby, EXPGUI, a graphical user interface for GSAS, J. Appl. Crystallogr. 34 (2001) 210–213.
[50] H. Rietveld, A profile refinement method for nuclear and magnetic structures, J. Appl. Crystallogr. 2 (1969) 65–71.
[51] V. Bakakin, R. Klevtsova, L. Gaponenko, Crystal-structure of magnesium molybdate $MgMoO_4$-An example of the modified closest packing with 2 types of tetrahedra, Kristallografiya 27 (1982) 38–42.
[52] M. Gemmi, M.G.I. La Placa, A.S. Galanis, E.F. Rauch, S. Nicolopoulos, Fast electron diffraction tomography, J. Appl. Crystallogr. 48 (2015) 718–727.
[53] Y.K. Egorovtismenko, M. Simonov, N. Belov, Crystal structure of $SrMoO_4$, Sov. Phys. Crystallogr. 12 (1967) 436.
[54] D. Errandonea, R.S. Kumar, X. Ma, C. Tu, High-pressure X-ray diffraction study of $SrMoO_4$ and pressure-induced structural changes, J. Solid State Chem. 181 (2008) 355–364.
[55] G.L. Messing, S.C. Zhang, G.V. Jayanthi, Ceramic powder synthesis by spray pyrolysis, J. Am. Ceram. Soc. 76 (1993) 2707–2726.
[56] W.M. Haynes, CRC Handbook of Chemistry and Physics, 97 ed., CRC Press, 2016.
[57] P.J. Miller, The Raman spectra of $MgMoO_4$, Spectrochim. Acta A Mol. Spectrosc 27 (1971) 957–960.
[58] M.N. Coelho, P.T.C. Freire, M. Maczka, C. Luz-Lima, G.D. Saraiva, W. Paraguassu, A.G. Souza Filho, P.S. Pizani, High-pressure Raman scattering of $MgMoO_4$, Vib. Spectrosc. 68 (2013) 34–39.
[59] A. Jayaraman, S.Y. Wang, S.R. Shieh, S.K. Sharma, L.C. Ming, High-pressure Raman study of SrMoO4 up to 37 GPa and pressure-induced phase transitions, J. Raman Spectrosc. 26 (1995) 451–455.
[60] D. Errandonea, L. Gracia, R. Lacomba-Perales, A. Polian, J.C. Chervin, Compression of scheelite-type $SrMoO_4$ under quasi-hydrostatic conditions: redefining the high-pressure structural sequence, J. Appl. Phys. 113 (2013) 123510.
[61] L. Tolvaj, K. Mitsui, D. Varga, Validity limits of Kubelka–Munk theory for DRIFT spectra of photodegraded solid wood, Wood Sci. Technol. 45 (2011) 135–146.
[62] D.L. Wood, J. Tauc, Weak absorption tails in amorphous semiconductors, Phys. Rev. B 5 (1972) 3144–3151.
[63] L.X. Lovisa, M.C. Oliveira, J. Andrés, L. Gracia, M.S. Li, E. Longo, R.L. Tranquilin, C.A. Paskocimas, M.R.D. Bomio, F.V. Motta, Structure, morphology and photoluminescence emissions of $ZnMoO_4$: RE^{3+}=Tb^{3+} - Tm^{3+} - X Eu^{3+} (x = 1, 1.5, 2, 2.5 and 3 mol%) particles obtained by the sonochemical method, J. Alloy. Comp. 750 (2018) 55–70.
[64] M. Pawlikowska, H. Fuks, E. Tomaszewicz, Solid state and combustion synthesis of Mn^{2+}-doped scheelites – their optical and magnetic properties, Ceram. Int. 43 (2017) 14135–14145.
[65] S. Dutta, S. Som, A.K. Kunti, V. Kumar, S.K. Sharma, H.C. Swart, H.G. Visser, Structural and luminescence responses of $CaMoO_4$ nano phosphors synthesized by hydrothermal route to swift heavy ion irradiation: elemental and spectral stability, Acta Mater. 124 (2017) 109–119.
[66] G.M. Gurgel, L.X. Lovisa, L.M. Pereira, F.V. Motta, M.S. Li, E. Longo, C.A. Paskocimas, M.R.D. Bomio, Photoluminescence properties of (Eu, Tb, Tm) co-doped $PbMoO_4$ obtained by sonochemical synthesis, J. Alloy. Comp. 700 (2017) 130–137.
[67] V. Panchal, N. Garg, H.K. Poswal, D. Errandonea, P. Rodríguez-Hernández, A. Muñoz, E. Cavalli, High-pressure behavior of $CaMoO_4$, Phys. Rev. Mater. 1 (2017) 043605.
[68] M.M.S. Silva, M.S. Sena, A.L. Lopes-Moriyama, C.P. Souza, A.G. Santos, Experimental planning of the synthesis of strontium molybdate by EDTA-citrate and its structural influence, morphology and optical bandgap, Ceram. Int. 44 (2018) 16606–16614.
[69] S. Wannapop, T. Thongtem, S. Thongtem, Fabrication of $MgMoO_4$–PVA and $MgMoO_4$ fibrous webs via a direct high voltage electrospinning process, J. Phys. Chem. Solids 74 (2013) 677–681.
[70] L. Zhang, W. He, K. Shen, Y. Liu, S. Guo, Controllable synthesis of hierarchical $MgMoO_4$ nanosheet-arrays and nano-flowers assembled with mesoporous ultrathin nanosheets, J. Phys. Chem. Solids 115 (2018) 215–220.
[71] R. Lacomba-Perales, J. Ruiz-Fuertes, D. Errandonea, D. Martínez-García, A. Segura, Optical absorption of divalent metal tungstates: correlation between the band-gap energy and the cation ionic radius, EPL (Europhys. Lett.) 83 (2008) 37002.
[72] L.D.S. Alencar, A. Mesquita, C.A.C. Feitosa, R. Balzer, L.F.D. Probst, D.C. Batalha, M.G. Rosmaninho, H.V. Fajardo, M.I.B. Bernardi, Preparation, characterization and catalytic application of Barium molybdate ($BaMoO_4$) and Barium tungstate ($BaWO_4$) in the gas-phase oxidation of toluene, Ceram. Int. 43 (2017) 4462–4469.
[73] M.F.C. Abreu, F.V. Motta, R.C. Lima, M.S. Li, E. Longo, A.P.d.A. Marques, Effect of process parameters on photophysical properties and barium molybdate phosphors characteristics, Ceram. Int. 40 (2014) 6719–6729.
[74] J.C. Sczancoski, L.S. Cavalcante, N.L. Marana, R.O. da Silva, R.L. Tranquilin, M.R. Joya, P.S. Pizani, J.A. Varela, J.R. Sambrano, M. Siu Li, E. Longo, J. Andrés, Electronic structure and optical properties of $BaMoO_4$ powders, Curr. Appl.

Phys. 10 (2010) 614–624.
[75] V.M. Longo, L.S. Cavalcante, E.C. Paris, J.C. Sczancoski, P.S. Pizani, M.S. Li, J. Andrés, E. Longo, J.A. Varela, Hierarchical assembly of $CaMoO_4$ nano-octahedrons and their photoluminescence properties, J. Phys. Chem. C 115 (2011) 5207–5219.
[76] G. Botelho, I.C. Nogueira, E. Moraes, E. Longo, Study of structural and optical properties of $CaMoO_4$ nanoparticles synthesized by the microwave-assisted solvothermal method, Mater. Chem. Phys. 183 (2016) 110–120.
[77] T. Thongtem, S. Kungwankunakorn, B. Kuntalue, A. Phuruangrat, S. Thongtem, Luminescence and absorbance of highly crystalline $CaMoO_4$, $SrMoO_4$, $CaWO_4$ and $SrWO_4$ nanoparticles synthesized by co-precipitation method at room temperature, J. Alloy. Comp. 506 (2010) 475–481.
[78] V.M. Longo, L.S. Cavalcante, A.T. de Figueiredo, L.P.S. Santos, E. Longo, J.A. Varela, J.R. Sambrano, C.A. Paskocimas, F.S. De Vicente, A.C. Hernandes, Highly intense violet-blue light emission at room temperature in structurally disordered $SrZrO_3$ powders, Appl. Phys. Lett. 90 (2007) 091906.
[79] V.S. Marques, L.S. Cavalcante, J.C. Sczancoski, A.F.P. Alcântara, M.O. Orlandi, E. Moraes, E. Longo, J.A. Varela, M. Siu Li, M.R.M.C. Santos, Effect of different solvent ratios (water/ethylene glycol) on the growth process of $CaMoO_4$ crystals and their optical properties, Cryst. Growth Des. 10 (2010) 4752–4768.
[80] V.M. Longo, A.T.d. Figueiredo, A.B. Campos, J.W.M. Espinosa, A.C. Hernandes, C.A. Taft, J.R. Sambrano, J.A. Varela, E. Longo, Different origins of green-light photoluminescence emission in structurally ordered and disordered powders of calcium molybdate, J. Phys. Chem. A 112 (2008) 8920–8928.
[81] M.T. Fabbro, C.C. Foggi, L.P.S. Santos, L. Gracia, A. Perrin, C. Perrin, C.E. Vergani, A.L. Machado, J. Andrés, E. Cordoncillo, E. Longo, Synthesis, antifungal evaluation and optical properties of silver molybdate microcrystals in different solvents: a combined experimental and theoretical study, Dalton Trans. 45 (2016) 10736–10743.
[82] Y. Ren, Z. Yang, M. Li, J. Ruan, J. Zhao, J. Qiu, Z. Song, D. Zhou, Reversible upconversion luminescence modification based on photochromism in $BaMgSiO_4:Yb^{3+},Tb^{3+}$ ceramics for anti-counterfeiting applications, Adv. Opt. Mater. 7 (2019) 1900213.
[83] J. Ruan, Z. Yang, A. Huang, H. Zhang, J. Qiu, Z. Song, Thermomchromic reaction-induced reversible upconversion emission modulation for switching devices and tunable upconversion emission based on defect engineering of $WO_3:Yb^{3+},Er^{3+}$ phosphor, ACS Appl. Mater. Interfaces 10 (2018) 14941–14947.
[84] S. Nizamoglu, G. Zengin, H.V. Demir, Color-converting combinations of nanocrystal emitters for warm-white light generation with high color rendering index, Appl. Phys. Lett. 92 (2008) 031102.
[85] A.A. Setlur, E.V. Radkov, C.S. Henderson, J.-H. Her, A.M. Srivastava, N. Karkada, M.S. Kishore, N.P. Kumar, D. Aesram, A. Deshpande, B. Kolodin, L.S. Grigorov, U. Happek, Energy-efficient, high-color-rendering led lamps using oxyfluoride and fluoride phosphors, Chem. Mater. 22 (2010) 4076–4082.
[86] V.C. Adya, M. Mohapatra, M.K. Bhide, V. Natarajan, Observation of “cool daylight” white light emission from Eu and Tb co-doped $SrMoO_4$ nano ceramics, Mater. Sci. Eng., B 203 (2016) 35–40.
[87] R. Cao, K. Chen, P. Liu, C. Cao, Y. Xu, H. Ao, P. Tang, Tunable photoluminescence properties of $Sr_{1-y}Ca_yMoO_4:Sm^{3+}$ phosphors ($0 \leq y < 1$), Luminescence 30 (2015) 962–966.
[88] L. Han, G. Liu, X. Dong, J. Wang, X. Wang, Y. Yang, A potential single-component white-light-emitting phosphor $CaMoO_4:La^{3+},Dy^{3+}$: hydrothermal synthesis, luminescence properties and energy transfer, J. Mater. Sci. Mater. Electron. 28 (2017) 16519–16526.
[89] M. Laguna, N.O. Nuñez, A.I. Becerro, M. Ocaña, Morphology control of uniform $CaMoO_4$ microarchitectures and development of white light emitting phosphors by Ln doping (Ln = Dy^{3+}, Eu^{3+}), CrystEngComm 19 (2017) 1590–1600.
[90] S. Das, P. Reed McDonagh, T. Selvan Sakthivel, S. Barkam, K. Killion, J. Ortiz, S. Saraf, A. Kumar, A. Gupta, J. Zweit, S. Seal, Tissue deposition and toxicological effects of commercially significant rare earth oxide nanomaterials: material and physical properties, Environ. Toxicol. 32 (2017) 904–917.
[91] K.T. Rim, K.H. Koo, J.S. Park, Toxicological evaluations of rare earths and their health impacts to workers: a literature review, Saf. Health Work 4 (2013) 12–26.